

Reactive oxygen species produced by NADPH oxidase regulate plant cell growth

Julia Foreman*†, Vadim Demidchik†‡, John H. F. Bothwell†§, Panagiota Mylona*, Henk Miedema‡, Miguel Angel Torres||¶, Paul Linstead*, Silvia Costa*, Colin Brownlee§, Jonathan D. G. Jones||, Julia M. Davies‡ & Liam Dolan*

* Department of Cell and Developmental Biology, John Innes Centre, Norwich NR4 7UH, UK

‡ Department of Plant Sciences, University of Cambridge, Cambridge CB2 3EA, UK

§ Marine Biological Association, Citadel Hill, Plymouth PL1 2PB, UK

|| Sainsbury Laboratory, John Innes Centre, Norwich NR4 7UH, UK

† These authors contributed equally to this work

Cell expansion is a central process in plant morphogenesis, and the elongation of roots and root hairs is essential for uptake of minerals and water from the soil. Ca^{2+} influx from the extracellular store is required for (and sets the rates of) cell elongation in roots¹. *Arabidopsis thaliana rhd2* mutants are defective in Ca^{2+} uptake and consequently cell expansion is compromised—*rhd2* mutants have short root hairs^{2,3} and stunted roots. To determine the regulation of Ca^{2+} acquisition in growing root cells we show here that RHD2 is an NADPH oxidase, a protein that transfers electrons from NADPH to an electron acceptor leading to the formation of reactive oxygen species (ROS). We show that ROS accumulate in growing wild-type (WT) root hairs but their levels are markedly decreased in *rhd2* mutants. Blocking the activity of the NADPH oxidase with diphenylene iodonium (DPI) inhibits ROS formation and phenocopies *Rhd2*⁻. Treatment of *rhd2* roots with ROS partly suppresses the mutant phenotype and stimulates the activity of plasma membrane hyperpolarization-activated Ca^{2+} channels, the predominant root Ca^{2+} acquisition system. This indicates that NADPH oxidases control development by making ROS that regulate plant cell expansion through the activation of Ca^{2+} channels.

Elevated concentrations of cytoplasmic free calcium ions ($[\text{Ca}^{2+}]_c$) stimulate exocytosis⁴ and support elongation of cells in roots¹. Ca^{2+} uptake for root growth is greatest in the elongation zone⁵ and is thought to be mediated by plasma membrane hyperpolarization-activated cation channels^{6–8}. In roots, once epidermal cells have stopped elongating, tip-growing root hairs elongate from specialized epidermal cells into the surrounding soil. All tip-growing cells (including pollen tubes, fungal hyphae and root hairs) transport Ca^{2+} across the plasma membrane into the tip, where the $[\text{Ca}^{2+}]_c$ is elevated compared with the rest of the cell. In *Arabidopsis* root hairs, the tip-high $[\text{Ca}^{2+}]_c$ gradient is first observed when slow tip growth initiates at a site on the root-hair bulge^{2,9}. Rapidly elongating root hairs maintain the $[\text{Ca}^{2+}]_c$ gradient until growth ceases when the gradient dissipates². No $[\text{Ca}^{2+}]_c$ gradient forms in *rhd2* mutants, which develop very short root hairs^{2,3} and stunted roots (mean \pm s.e.m. root length at 8 days: WT, 25.1 ± 0.7 mm; *rhd2*, 19.9 ± 0.5 mm, $n = 100$; significant at the 99.9% level, Student's *t*-test), indicating that RHD2 is required for the establishment of Ca^{2+} -mediated cell growth² (Fig. 1a and b).

We cloned RHD2 by transposon tagging with the Spm-induced *rhd2-4* allele. DNA flanking the transposon was isolated by inverse polymerase chain reaction (PCR) and sequenced. This showed that the Spm element was inserted into the gene At5g51060 (TIGR;

GenBank accession number AF055355) where it caused a three-base pair duplication of bases 4151–4153 (Fig. 1c). We identified single G to A point mutations in three other mutant alleles, converting tryptophan residues to premature stop codons at positions 597, 737 and 815 in *rhd2-1*, *rhd2-2* and *rhd2-3*, respectively (Fig. 1c). We complemented plants homozygous for the *rhd2-4* mutation with an 8.4-kilobase *Hind*III–*Bgl*II genomic fragment that includes the entire At5g51060 gene, its native promoter and 700 base pairs (bp) of 3' DNA (Fig. 1c). In the T₂ generation, the kanamycin resistance of the T-DNA marker co-segregated with the WT root-hair phenotype. Taken together, these data indicate that the *Rhd2*⁻ mutant phenotype is caused by the mutation in the At5g51060 gene. At5g51060 had previously been defined as *Arabidopsis thaliana respiratory burst oxidase homolog C* (*AtrbohC*)^{10,11}. This gene hereafter is designated ROOT HAIR DEFECTIVE2/*Arabidopsis thaliana respiratory burst oxidase homolog C* (*RHD2/AtrbohC*). *RHD2/AtrbohC* transcript is present in the epidermis in the proximal regions of the meristem, in the elongation zone, in the differentiation zone and in elongating root hairs (Fig. 1d–j).

Arabidopsis thaliana respiratory burst oxidase homologues (*Atrboh*) are homologous to gp91^{phox}, the glycosylated transmembrane subunit of the mammalian NADPH oxidase cytochrome that catalyses ROS production^{10–12}. There are 10 *Atrboh*s in *Arabidopsis*. The proteins have an approximately 300-residue cytoplasmic amino-terminal region containing two putative EF-hand motifs,

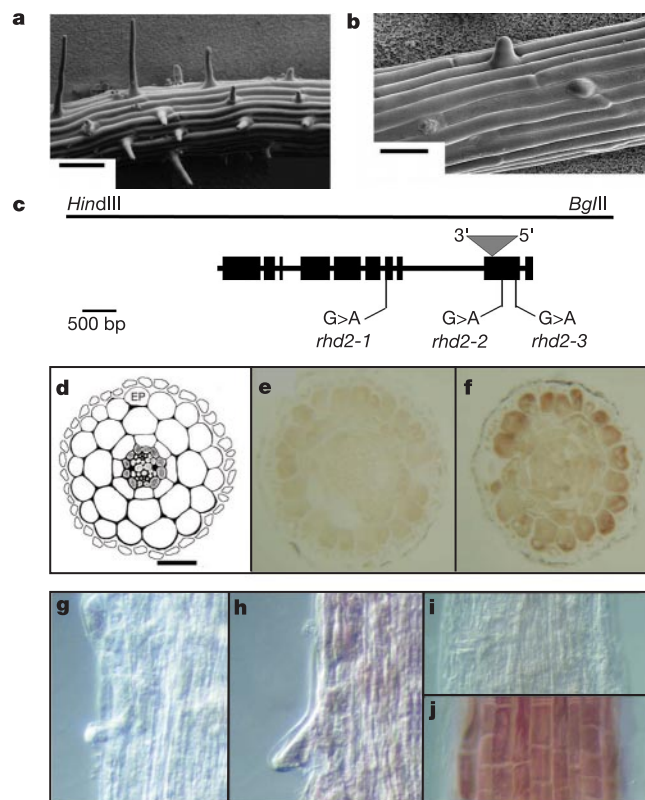


Figure 1 Characterization of *RHD2/AtrbohC* gene. **a**, WT (scale bar, 100 μm). **b**, *rhd2* mutant (scale bar, 50 μm). **c**, *RHD2* is located on chromosome 5 on TAC clone K3K7. The intron–exon organization of *RHD2/AtrbohC* and the positions of *rhd2-1*, *rhd2-2*, *rhd2-3* and *rhd2-4* (grey triangle) mutations are shown. **d**, Schematic transverse section, showing the epidermis (EP) (scale bar, 25 μm). **e**, *In situ* hybridization of *RHD2/AtrbohC* sense probe (control). **f**, Antisense *RHD2/AtrbohC* probe. **g**, *In situ* hybridization of *RHD2/AtrbohC* sense (control). **h**, Antisense *RHD2/AtrbohC* probe in the region where root hairs grow. **i**, *In situ* hybridization of *RHD2/AtrbohC* sense probe (control). **j**, Antisense *RHD2/AtrbohC* probe shows that *RHD2* is expressed in the elongation zone.

¶ Present address: Department of Biology and Curriculum in Genetics and Molecular Biology, CB3280, 108 Coker Hall, University of North Carolina, Chapel Hill, NC 27599-3280, USA.

indicating a direct regulatory effect of Ca^{2+} ions^{10,11}. *AtrbohD* and *AtrbohF* have been shown to produce ROS in response to pathogen infection¹³ but so far no developmental roles for *Atrboh*s have been reported.

To correlate RHD2/*AtrbohC*-mediated ROS production with growth, a lucigenin chemiluminescence assay of ROS production¹⁴ was used. *rhb2* excised root apices (3–4 cm from apex, 10–20 mg fresh weight) produced about half the amount of ROS formed by WT (mean \pm s.e.m. counts $\text{s}^{-1} \text{mg}^{-1}$: WT, 3.6 ± 0.6 ; *rhb2*, 1.54 ± 0.46 ; $n = 4$), which is consistent with impaired NADPH oxidase activity in the *rhb2* mutant. To image ROS within developing hair cells we ester-loaded 5-(and 6)-chloromethyl-2',7'-

dichlorodihydrofluorescein (CM-H₂DCF), a ROS-sensitive dye with good intracellular retention into growing roots. Figure 2a shows the increase in ROS within a WT root hair as it emerges initially as a bulge and then elongates by tip growth over the course of an hour. In contrast, there was no ROS accumulation in the *rhb2* root-hair bulge over the same period (Fig. 2b; see Supplementary Information for dye-loading control experiments). For WT, both the ROS production at the apex of the root-hair bulge and the elongation rate increased with time ($n = 8$; Fig. 2d and e), whereas *rhb2* was impaired in both ROS accumulation and elongation ($n = 3$, Fig. 2d and e). Application of 50 μM diphenylene iodonium (DPI), an inhibitor of NADPH oxidase and other flavin-containing enzymes¹⁵, prevented ROS accumulation in, and elongation of, WT root-hair bulges ($n = 5$; Fig. 2f–h). The fact that treatment of WT with DPI phenocopies *Rhd2*⁻ supports the view that an NADPH oxidase is required for root-hair growth. In addition, application of 10 μM DPI to WT inhibited the extension rate of the primary root (measured between 7 and 14 days of growth) by nearly 70% (mean \pm s.e.m., mm d^{-1} : control, 3.9 ± 0.3 ; DPI-treated root, 1.2 ± 0.2 ; $n = 10$). Taken together, the data indicate that the RHD2/*AtrbohC* protein is required for producing ROS throughout the root and that ROS are required for both root and root-hair growth.

Because *rhb2* mutants are defective in setting up the tip-high Ca^{2+} gradient in root hairs we propose that ROS produced by the activity of RHD2 are required to stimulate Ca^{2+} influx during hair elongation and cell extension^{6–8}. It follows that the application of ROS to *rhb2* root-hair bulges might elevate $[\text{Ca}^{2+}]_c$. During

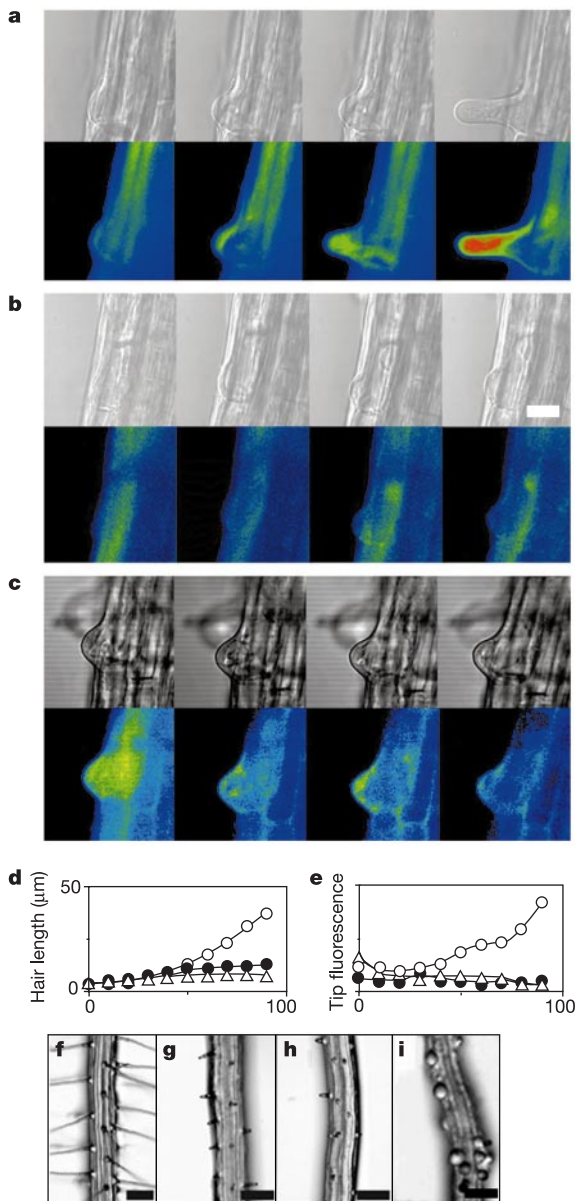


Figure 2 ROS accumulation (CM-H₂DCF imaging) during root-hair elongation: transmission (top) and pseudocolour fluorescent images (bottom) are displayed for WT (**a**), *rhb2* (**b**) and WT (**c**) after treatment with DPI. Scale bar in **b**, 20 μm (applies to **a–c**). Red indicates high concentration; blue indicates low concentration. **d**, Increase in root-hair length (mean \pm s.e.m.); **e**, increase in ROS (arbitrary units) at the hair apex. Open circles, WT, ($n = 8$); filled circles, *rhb2* ($n = 3$); open triangles, WT with 50 μM DPI added at zero time ($n = 5$). **f**, WT roots; **g**, *rhb2* roots. **h**, WT with 50 μM DPI. **i**, OH⁻-treated *rhb2* (Scale bar in **f–i**, 100 μm).

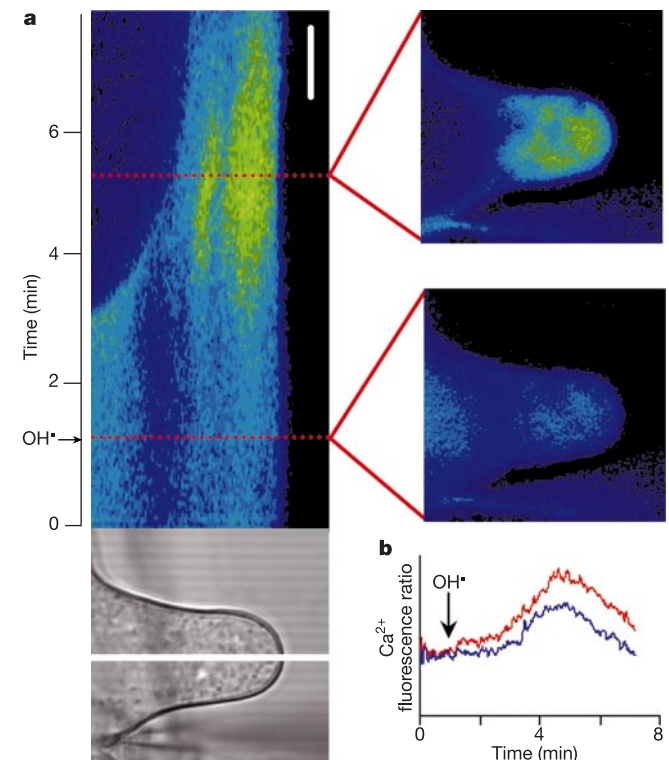


Figure 3 ROS elevates $[\text{Ca}^{2+}]_c$ in a *rhb2* root-hair bulge. **a**, Left, time course of changes in the calcium green/Texas red pseudocolour Ca^{2+} fluorescence ratio for the linescan bar (30 μm) shown in the transmission image of an *rhb2* bulge. Right lower panel, image obtained immediately before the addition of OH⁻; right upper panel, image obtained 3.5 min after addition. Red indicates high concentration; blue indicates low concentration. **b**, Time course of changes Ca^{2+} fluorescence ratio in apical (red; 2 μm back from the extreme tip) and sub-apical (blue; 10 μm back from the extreme tip) regions of the bulge. Arrow indicates the time of addition of OH⁻.

endogenous ROS elevation, the superoxide anion produced by a plasma membrane NADPH oxidase can be converted to H_2O_2 by superoxide dismutase in the plant apoplast. Hydrogen peroxide (which is known to activate guard-cell Ca^{2+} channels¹⁶) can then be readily converted to hydroxyl radicals (OH^\cdot) in the presence of transition metals (such as Cu^{2+} or Fe^{2+})^{17,18}. OH^\cdot are the most reactive ROS and interact directly with most target biomolecules¹⁸. Here, OH^\cdot were generated by applying a mixture of 2 mM H_2O_2 , 0.2 mM Cu^{2+} and 0.2 mM ascorbate¹⁸. As shown in Fig. 3, application of OH^\cdot to *rhd2* root-hair bulges caused a rapid elevation in $[Ca^{2+}]_c$ ($n = 4$; reported by confocal imaging of calcium green normalized to Texas red). This $[Ca^{2+}]_c$ elevation was either delocalized or tip-high (Fig. 3b), which is consistent with OH^\cdot treatment's restoring the WT $[Ca^{2+}]_c$ gradient. To demonstrate that ROS elevated $[Ca^{2+}]_c$ by activating a plasma membrane Ca^{2+} influx pathway, spheroplasts were released by laser microsurgery from the apices of WT young root hairs and *rhd2* bulges, then ester-loaded with calcium green-1 acetoxymethyl ester, a non-ratiometric Ca^{2+} -reporting fluoroprobe. OH^\cdot again elevated $[Ca^{2+}]_c$ but this was prevented by the application of 0.1 mM Gd^{3+} (a Ca^{2+} -channel

antagonist; data in Supplementary Information). Moreover, increasing ROS levels in *rhd2* roots by treatment with OH^\cdot led to depolarized root-hair growth—hairs expanded on all surfaces, leading to the formation of spherical outgrowths (Fig. 2i). The formation of non-polarized hairs upon homogeneous treatment with OH^\cdot suggests that the polarized production of ROS is required for the formation of a polarized hair outgrowth.

Because these data suggest that ROS elevate $[Ca^{2+}]_c$ by means of Ca^{2+} influx we tested for ROS activation of plasma membrane Ca^{2+} channels in protoplasts derived from the elongation zone epidermis and in apical spheroplasts isolated from root hairs. With the use of the whole-cell patch clamp configuration, no significant Ca^{2+} conductance was evident in WT protoplasts from elongation zone epidermis under control conditions (Fig. 4a). In all protoplasts tested, a Ca^{2+} -permeable, inwardly rectifying, hyperpolarization-activated conductance appeared within a few minutes of exposure to the OH^\cdot -generating mixture and attained its maximum 20–40 min after exposure ($n = 4$). No activation was achieved by the addition of either 2 mM H_2O_2 or 0.2 mM Cu^{2+} or 0.2 mM ascorbate individually (data not shown). The OH^\cdot -activated conductance was

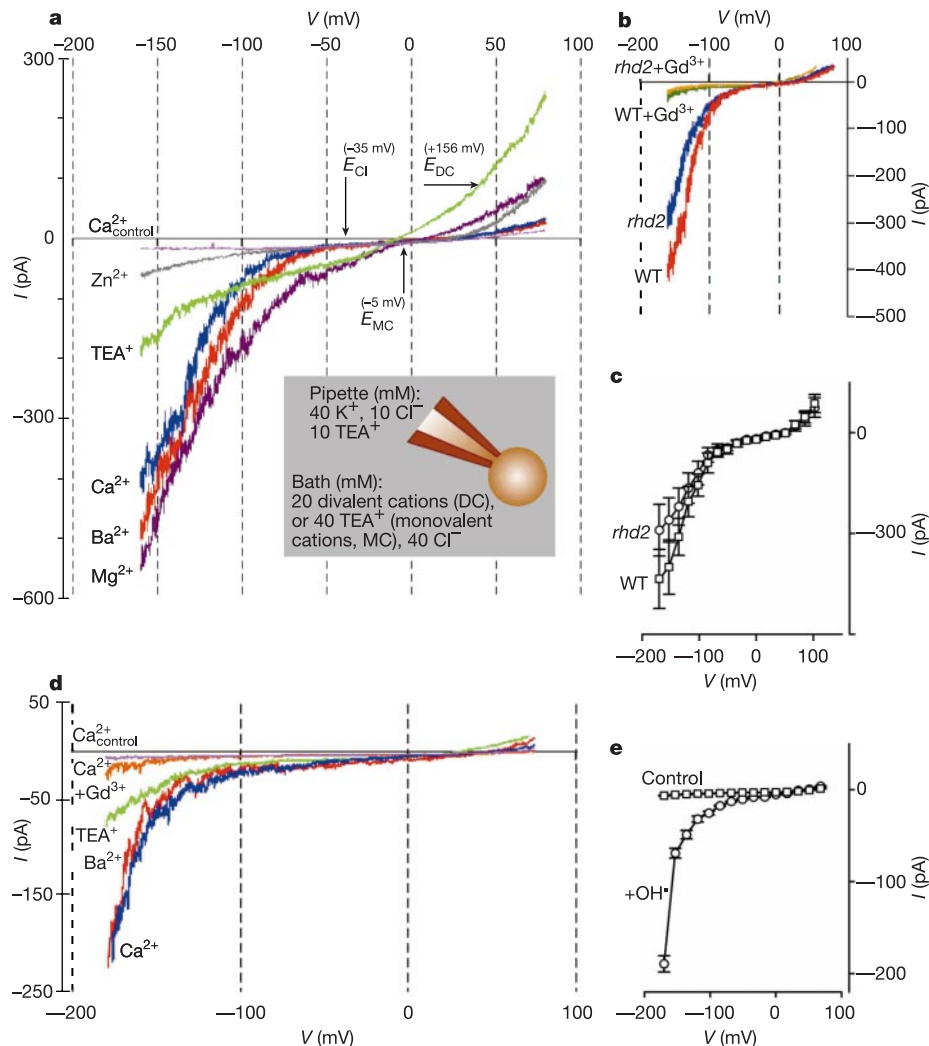


Figure 4 Activation of hyperpolarization-activated Ca^{2+} channels by ROS. **a**, Whole-cell currents from a WT elongation zone epidermal protoplast. After activation by OH^\cdot in 20 mM external Ca^{2+} , the protoplast was exposed to different cations in the presence of OH^\cdot . E is the estimated equilibrium potential. **b**, OH^\cdot -activated Ca^{2+} currents from a WT and an *rhd2* elongation-zone epidermal protoplast. **c**, Mean (\pm s.e.m.) current–voltage

$I-V$ relationships for elongation-zone OH^\cdot -activated Ca^{2+} currents; $n = 4$. **d**, OH^\cdot activation of whole-cell currents from a WT hair apical spheroplast. Protocol and equilibrium potentials as in **a**. **e**, Mean (\pm s.e.m.) $I-V$ relationships for WT hair OH^\cdot -activated Ca^{2+} currents; $n = 7$. In **b**, **c** and **e** the bath contained 20 mM Ca^{2+} .

readily permeable to divalent cations (Fig. 4a) including Ba^{2+} , indicating that this was a Ca^{2+} conductance rather than the inwardly rectifying K^+ channel conductance in the root¹⁹. The K^+ channel blocker tetraethylammonium (TEA^+) permeated the OH^- -activated conductance but Zn^{2+} permeation was poor (Fig. 4a), which is consistent with the operation of a Ca^{2+} conductance²⁰. External Gd^{3+} (0.1 mM) blocked the conductance (Fig. 4b). Application of 0.1 and 1 mM $GdCl_3$ to WT root apices decreased root elongation rate (4–8-day application and growth interval, mean \pm s.e.m., $mm\ d^{-1}$: control 10.9 ± 0.4 , $n = 35$; 0.1 mM Gd^{3+} , 7.4 ± 0.3 , $n = 52$; 1 mM Gd^{3+} , 4.38 ± 0.4 , $n = 41$), supporting a role for this OH^- -activated Ca^{2+} conductance in growth. Chelation of extracellular Ca^{2+} by the apical application of 10 mM BAPTA caused a 10-fold decrease in growth rate (control, 10.8 ± 0.3 , $n = 65$; BAPTA, 1.1 ± 0.1 , $n = 90$), confirming Ca^{2+} uptake as essential. The OH^- -induced hyperpolarization-activated Ca^{2+} conductance was found in all protoplasts derived from the elongation-zone epidermis of *rhd2* (Fig. 4b and c; $n = 4$). As there was no significant difference in the current amplitudes of the OH^- -induced conductance between *rhd2* and WT protoplasts (Fig. 4c; $n = 4$, recorded in 20 mM Ca^{2+}), the intrinsic sensitivity of the underlying Ca^{2+} channel to ROS and the number of channel proteins seem not to be affected by the *rhd2* mutation.

Application of OH^- (generated in these experiments by 0.5 mM Cu^{2+} and 0.5 mM ascorbate¹⁸) to WT root-hair apical spheroplasts also activated an inwardly rectifying, hyperpolarization-activated conductance in the plasma membrane. This conductance was mediated by Ca^{2+} , Ba^{2+} and TEA^+ (Fig. 4d and e; $n = 7$). Activation was apparent within 5 min of the application of OH^- and attained a maximum within 30 min. No channel activation was observed after the addition of 0.5 mM Cu^{2+} alone. The root-hair ROS-activated Ca^{2+} conductance was blocked by 0.1 mM Gd^{3+} (Fig. 4d), strongly suggesting that this Ca^{2+} influx pathway was responsible for the ROS-induced Gd^{3+} -sensitive elevation in $[Ca^{2+}]_c$ observed in isolated apical spheroplasts (Supplementary Information). Significantly, lanthanides (which block Ca^{2+} channels) inhibit root-hair elongation²¹. These data indicate that the defect in ROS production in the *rhd2* mutant compromises the ROS-activated plasma membrane Ca^{2+} -channel influx mechanism required for root-hair cell elongation. Our data also indicate that the same mechanism might operate during expansive cell elongation found in other cell types. The involvement of ROS in both types of cell elongation can account for the short root and root-hairless phenotypes characteristic of the *rhd2* mutant.

The demonstration that ROS can activate Ca^{2+} channels in the root combined with *rhd2* root-elongation defects indicates that RHD2/*AtrbohC* is part of the mechanism controlling cell expansion. The animal NADPH oxidase gp91^{phox} is regulated by Rac proteins, and similar proteins in plants called Rops ('Rho-related GTPases from plants') have been shown to be involved in correct cellular expansion in the root elongation zone, the establishment of the tip-high Ca^{2+} gradient and root-hair growth^{12,22,23}. We therefore propose that a Rop protein activates RHD2/*AtrbohC* and the resultant ROS (as OH^-) then activate the hyperpolarization-activated Ca^{2+} channels to facilitate Ca^{2+} influx for growth, where it is involved in the modulation of actin dynamics and other processes required for growth. The production of ROS in the growing region of the hair cell indicates that local ROS formation might be part of the mechanism that establishes hair polarity. □

Methods

Plants and growth conditions

Arabidopsis thaliana (L.) Heyn. lines used in these experiments were derived from the Landsberg *erecta* and Columbia backgrounds. Plants were grown vertically on MS medium (solidified with Phytigel) at 24 °C under continuous illumination. Seedlings were grown to maturity on a 1:1 mix of potting compost (John Innes no. 1) and peat moss.

Sequencing of mutant alleles

To sequence *rhd2* alleles, the RHD2/*AtrbohC* genomic sequence from WT and mutant plant tissues was amplified by PCR with a mix of *Taq* DNA polymerase (Gibco BRL) and *Pfu* DNA polymerase (Promega). Nucleotide sequences were determined with the ABI PRISM® BigDye™ Terminator Cycle Sequencing Ready Reaction Kit (Applied Biosystems) in conjunction with an Applied Biosystems 3700 DNA sequencer. Sequences were analysed with LASERGENE computer software.

Inverse PCR and reverse transcriptase-mediated PCR analysis

Genomic DNA was isolated from 6-week-old plants. Inverse PCR was performed as described in ref. 24. *AtrbohC* transcript levels were tested with PCR primers BO1 (5'-GAAGTGTCCAGGAGGCTATCACTCTGA-3') and BO2 (5'-GCAAAATCCTTTGAAGTCATCC-3') and were run with the following temperature profile (40 cycles): 2 min at 94 °C, 30 s at 94 °C, 44 s at 55 °C, 1 min at 72 °C. These primers produce a 559-bp fragment when complementary DNA is used as the template and a 640-bp fragment when genomic DNA is used.

In situ hybridization

A 660-bp fragment of genomic TAC clone K3K7, spanning the first intron and first exon of RHD2/*AtrbohC*, was cloned into pBluescript SK⁺. The antisense probe was transcribed with T3 RNA polymerase; the sense probe was transcribed with T7. *In situ* hybridization of digoxigenin-UTP-labelled RNA probes were performed as described²⁵. For *in situ* hybridization of sectioned material, we performed tissue fixation, wax embedding and tissue sectioning as described²⁵.

Constructs and plant transformation

For the complementation of *rhd2* a *HindIII*-*BglII* fragment from genomic TAC clone K3K7, containing the full-length RHD2/*AtrbohC* gene, 2,750 bp of its promoter and 700 bp downstream, was cloned into a binary vector. This construct was introduced in *Agrobacterium tumefaciens* strain GV3101 using triparental mating and was transformed into homozygous *rhd2-4* mutant or WT plants by infiltration.

Sequence analysis

The BLAST search program was used for sequence analysis and comparisons in the Tair, GenBank, EMBL and SwissProt databases²⁶. Multiple sequence alignments and a phylogenetic tree based on pairwise dynamic alignment were done with ClustalW (Des Higgins) and TreeViewPPC v. 1.6.2 programs^{27,28}. The sequences of *Atrboh*s and gp91^{phox} were accessed from GenBank.

Production of protoplasts and spheroplasts

Root tips were exposed to enzyme solution (1.5% cellulase, 1% cellulysin, 0.1% pectolyase, 0.1% bovine serum albumin, 10 mM KCl, 10 mM $CaCl_2$, 2 mM $MgCl_2$, 2 mM MES, adjusted to pH 5.7 with Tris base, and to 290–300 mosM with sorbitol) for 1–2 h (22 °C) to release elongation-zone epidermal protoplasts (diameter 20 μ m). Apical spheroplasts were released from hairs by laser ablation⁷ or by enzymatic digestion of the cell wall (1.5–2 h) of roots from which the tip (containing the elongation zone) had been removed. No release of epidermal protoplasts was observed. Both methods yielded densely cytoplasmic spheroplasts (diameter 12–14 μ m), typical of young root hairs⁷.

Imaging

Plants 4–5 days old were used, and all fluorescence images were obtained with a Nikon Diaphot 300 inverted microscope coupled to a MRC 1024 scanning-laser confocal system (running Bio-Rad LaserSharp 2.1T). For experiments with $CM-H_2DCF$, roots were incubated for 60 min at 4 °C in 5–20 μ M $CM-H_2DCF$ diacetate, acetyl ester²⁹, dissolved in DMSO (less than 0.005% final concentration), then washed with 0.1 mM KCl, 0.1 mM $CaCl_2$ (pH 6.0) and left for 60 min at 22 °C before experimentation. Dye excitation was at 488 nm; emitted light was detected at 522 nm. Each image consisted of 512 \times 512 pixels, representing ten scans of 1 s each, and averaged with Kalman filtering. For cellular measurements of $[Ca^{2+}]_c$, microinjection pipettes were fabricated from 1.5-mm borosilicate pipettes and backfilled with 1 mM calcium green dextran (10 kDa) and 1 mM Texas red dextran (10 kDa). After impalement and recording of a stable membrane potential (measured with a discontinuous current clamp; Axoclamp 2B amplifier from Axon Instruments), pressure was applied (PLI 100 pressure injection system from Medical Systems Corp.) to ~250 kPa. Application of positive potential (+30 to +50 mV) facilitated dye injection by electro-osmotic flow. The impalement pipette was not removed. Cells were bathed in 0.1 mM KCl, 0.1 mM $CaCl_2$ (pH 6.0). Calcium green and Texas red fluorescence was monitored at 523 and 606 nm after excitation at 488 and 568 nm, respectively. Image pairs were collected at 1–3-s intervals and analysed with Scion Image software (Scion Corp., Frederick, MD). For cryoscanning electron microscopy, seedlings were placed on moist nitrocellulose paper, mounted on a stub and immersed in liquid nitrogen slush. Roots were transferred to a cold stage. After removal of water by sublimation, roots were sputter coated with gold and observed with a Jeol scanning electron microscope at -147 °C.

Electrophysiology

The bathing solution comprised (in mM): 20 mM chloride salt of Ca^{2+} , Ba^{2+} , Mg^{2+} or Zn^{2+} , or 40 mM TEACl with 2 mM MES (adjusted to pH 5.6 with Tris base, and to 290–300 mosM with sorbitol). Pipette solution contained (in mM): 40 K^+ , 10 TEA^+ , 10 Cl^- , 40 gluconate, 5 BAPTA (free Ca^{2+} adjusted to 100 nM with $Ca(OH)_2$), adjusted to pH 7.2 with 5 mM HEPES/NaOH. OH^- were generated by the addition of (in mM) either 2 H_2O_2 , 0.2 $CuCl_2$, 0.2 ascorbate or 0.5 $CuCl_2$, 0.5 ascorbate¹⁸. Standard patch clamping procedures were employed⁷. For voltage ramps, the holding voltage was -70 mV; then,

after a 10-s pre-pulse of +80 or +100 mV the voltage was ramped down to -180 mV over 42 s. Data were sampled at 2–5 kHz and low-pass filtered at 1–2 kHz.

Received 18 September 2002; accepted 5 February 2003; doi:10.1038/nature01485.

1. Cramer, G. R. & Jones, R. L. Osmotic stress and abscisic acid reduce cytosolic calcium activities in roots of *Arabidopsis thaliana*. *Plant Cell Environ.* **19**, 1291–1298 (1996).
2. Wymer, C. L., Bibikova, T. N. & Gilroy, S. Cytoplasmic free calcium distributions during the development of root hairs of *Arabidopsis thaliana*. *Plant J.* **12**, 427–439 (1997).
3. Schiefelbein, J. W. & Somerville, C. Genetic control of root hair development in *Arabidopsis thaliana*. *Plant Cell* **2**, 235–243 (1990).
4. Carroll, A. D. *et al.* Ca²⁺, annexins, and GTP modulate exocytosis from maize root cap protoplasts. *Plant Cell* **10**, 1267–1276 (1998).
5. Demidchik, V. *et al.* *Arabidopsis thaliana* root nonselective cation channels mediate calcium uptake and are involved in growth. *Plant J.* **32**, 799–808 (2002).
6. Kiegle, E., Gilliam, M., Haseloff, J. & Tester, M. Hyperpolarisation-activated calcium channels found only in cells from the elongation zone of *Arabidopsis thaliana* roots. *Plant J.* **21**, 225–229 (2000).
7. Véry, A.-A. & Davies, J. M. Hyperpolarization-activated calcium channels at the tip of *Arabidopsis* root hairs. *Proc. Natl Acad. Sci. USA* **97**, 9801–9806 (2000).
8. Miedema, H., Bothwell, J. H. F., Brownlee, C. & Davies, J. M. Calcium uptake by plant cells—channels and pumps acting in concert. *Trends Plant Sci.* **11**, 514–519 (2001).
9. Dolan, L. *et al.* Clonal relationships and cell patterning in the root epidermis of *Arabidopsis*. *Development* **120**, 2465–2474 (1994).
10. Keller, T. *et al.* A plant homolog of the neutrophil NADPH oxidase gp91^{phox} subunit gene encodes a plasma membrane protein with Ca²⁺ binding motifs. *Plant Cell* **10**, 255–266 (1998).
11. Torres, M. A. *et al.* Six *Arabidopsis thaliana* homologues of the human respiratory burst oxidase (gp91^{phox}). *Plant J.* **14**, 365–370 (1998).
12. Segal, A. W. & Abo, A. The biochemical basis of the NADPH oxidase of phagocytes. *Trends Biochem. Sci.* **18**, 43–47 (1993).
13. Torres, M. A., Dangel, J. L. & Jones, J. D. *Arabidopsis* gp91^{phox} homologues AtrbohD and AtrbohF are required for accumulation of reactive oxygen intermediates in the plant defence response. *Proc. Natl Acad. Sci. USA* **99**, 517–522 (2002).
14. Williams, A. J. & Cole, P. J. Investigation of alveolar macrophage function using luciferin-dependent chemiluminescence. *Thorax* **36**, 866–869 (1981).
15. Bolwell, G. P. & Wojtaszek, P. Mechanisms for the generation of reactive oxygen species in plant defence—a broad perspective. *Physiol. Mol. Plant Pathol.* **51**, 347–366 (1997).
16. Pei, Z. M. *et al.* Calcium channels activated by hydrogen peroxide mediate abscisic acid signalling in guard cells. *Nature* **406**, 731–734 (2000).
17. Fry, S. C. Oxidative scission of plant cell wall polysaccharides by ascorbate-induced hydroxyl radicals. *Biochem. J.* **332**, 507–515 (1998).
18. Halliwell, B. & Gutteridge, J. M. C. *Free Radicals in Biology and Medicine* (Oxford Univ. Press, Oxford, 1999).
19. Hirsch, R. E., Lewis, B. D., Spalding, E. P. & Sussman, M. R. A role for the AKT1 potassium channel in plant nutrition. *Science* **280**, 918–921 (1998).
20. Kiss, T. & Osipenko, O. N. Toxic effects of heavy metals on ionic channels. *Pharmacol. Rev.* **46**, 245–267 (1994).
21. Felle, H. & Hepler, P. K. The cytosolic Ca²⁺ concentration gradient of *Sinapis alba* root hairs as revealed by Ca²⁺-selective microelectrode tests and fura-dextran ratio imaging. *Plant Physiol.* **114**, 39–45 (1997).
22. Molendijk, A. J. *et al.* *Arabidopsis thaliana* Rop GTPases are localized to tips of root hairs and control polar growth. *EMBO J.* **20**, 2779–2788 (2001).
23. Jones, M. A. *et al.* The *Arabidopsis* Rop2 GTPase is a positive regulator of both root hair initiation and tip growth. *Plant Cell* **14**, 763–776 (2002).
24. Tissier, A. F. *et al.* Multiple independent defective *Suppressor-mutator* transposon insertions in *Arabidopsis*: A tool for functional genomics. *Plant Cell* **11**, 1841–1852 (1999).
25. Coen, E. S. *et al.* *floricaula*: a homeotic gene required for flower development in *Antirrhinum majus*. *Cell* **63**, 1311–1322 (1990).
26. Altschul, S. F. *et al.* Gapped BLAST and PSI-BLAST: A new generation of protein database search programs. *Nucleic Acids Res.* **25**, 3389–3402 (1997).
27. Thompson, J. D., Higgins, D. G. & Gibson, T. J. CLUSTAL W: Improving the sensitivity of progressive multiple sequence alignment through sequence weighting, position-specific gap penalties and weight matrix choice. *Nucleic Acids Res.* **22**, 4673–4680 (1994).
28. Page, R. D. M. TREEVIEW: An application to display phylogenetic trees on personal computers. *Computer Applic. Biosci.* **12**, 357–358 (1996).
29. Zhang, W. H., Rengel, Z. & Kuo, J. Determination of intracellular Ca²⁺ in cells of intact wheat roots: loading of acetoxymethyl ester of Fluo-3 under low temperature. *Plant J.* **15**, 147–151 (1998).

Supplementary Information accompanies the paper on Nature's website (<http://www.nature.com/nature>).

Acknowledgements We thank D. Graham and A. Dark for help with screening and cultivation, respectively; E. Ryan, P. Shaw and K. Roberts for comments on the manuscript; and P. Doerner for support. This work was funded by the BBSRC, the Gatsby Foundation, the Leverhulme Trust and the European Union.

Competing interests statement The authors declare that they have no competing financial interests.

Correspondence and requests for materials should be addressed to L.D. (e-mail: liam.dolan@bbsrc.ac.uk).

Hidden complexity in the mechanical properties of titin

Philip M. Williams*, Susan B. Fowler†, Robert B. Best†, José Luis Toca-Herrera†‡, Kathryn A. Scott†, Annette Steward† & Jane Clarke†

* Laboratory of Biophysics and Surface Analysis, School of Pharmaceutical Sciences, University of Nottingham, Nottingham NG7 2RD, UK
 † Cambridge University Chemical Laboratory, MRC Centre for Protein Engineering, Lensfield Road, Cambridge CB2 1EW, UK

Individual molecules of the giant protein titin span the A-bands and I-bands that make up striated muscle. The I-band region of titin is responsible for passive elasticity in such muscle^{1–4}, and contains tandem arrays of immunoglobulin domains. One such domain (I27) has been investigated extensively, using dynamic force spectroscopy and simulation^{5–12}. However, the relevance of these studies to the behaviour of the protein under physiological conditions was not established. Force studies reveal a lengthening of I27 without complete unfolding, forming a stable intermediate that has been suggested to be an important component of titin elasticity⁶. To develop a more complete picture of the forced unfolding pathway, we use mutant titins—certain mutations allow the role of the partly unfolded intermediate to be investigated in more depth. Here we show that, under physiological forces, the partly unfolded intermediate does not contribute to mechanical strength. We also propose a unified forced unfolding model of all I27 analogues studied, and conclude that I27 can withstand higher forces in muscle than was predicted previously.

Titin's I-band region is largely composed of tandem arrays of immunoglobulin domains along with the PEVK region, believed to be largely unstructured^{13–16}. Most studies suggest that under physiological forces the increase in the length of titin derives from straightening of the immunoglobulin regions and unfolding of the PEVK domains^{3,17}, although it has also been suggested that, at extremes of force, a small number of the immunoglobulin domains could unfold^{18,19}. The resistance of these immunoglobulin domains to force has been studied extensively by single-molecule studies^{5,10,20–22} that mostly used atomic force microscopy (AFM) techniques. They have been shown to be the most mechanically stable proteins studied to date, at the high loading rates of the experimental regime. However, extrapolation of these data to low loading rates that are likely to be physiologically relevant suggests that there will be considerable unfolding of the immunoglobulin domains. This is hard to reconcile with results that suggest that these domains are very stable in the intact sarcomere, and that they are likely to unfold very rarely *in vivo*^{3,17,23}. To understand fully how the immunoglobulin domains resist force, it is important to investigate in detail how the unfolding energy landscape responds to the application of force—in particular, to ask how it will respond to the low forces relevant to physiological conditions.

I27 (Fig. 1) unfolds through an intermediate (I) under force in which the A-strand is detached. This intermediate was first observed in modelling studies¹¹, confirmed by careful analysis of AFM traces⁶, and has been characterized by biophysical and structural techniques⁹. However, it is not observed in chemical denaturation studies²⁴. Force versus extension curves of wild-type (WT) I27 indicate that molecular rearrangement to I occurs around 100 pN (ref. 6), and as at AFM loading rates the WT unfolds above this force, the dynamic force spectrum for WT I27 represents the I to U transition (Fig. 2a): that is, this intermediate is the dominant species

‡ Present address: Center for Ultrastructure Research, Universität für Bodenkultur Wien, Gregor Mendel Strasse 33, A-1180 Vienna.